Noise Mechanisms Impacting Micro-Doppler Lidar Signals: Theory and Experiment

April 2000

Philip Gatt, Sammy W. Henderson, J. Alex Thomson and Stephen M. Hannon

Coherent Technologies, Inc.
655 Aspen Ridge Dr.
Lafayette, Colorado USA
Voice: (303) 604-2000, Fax: (303)-604-2500, e-mail: philg@ctilidar.com

ABSTRACT

Lidar remote sensing of micro-Doppler signals is important for many military applications including characterization and identification of ground and airborne targets (NCTID) and battle damage assessment. The single most important performance metric of these sensors is their velocity measurement precision. The velocity precision of a micro-Doppler lidar is limited by any one of various noise sources, which include shot-noise, local-oscillator frequency noise, speckle decorrelation noise and refractive turbulence piston noise. In this paper, we present a theory, which describes these noise sources and their wavelength dependence. For example, it will be shown that the turbulence piston noise is wavelength independent, while the wavelength dependence of speckle decorrelation noise depends upon whether or not the target is resolved. Furthermore, the noise sources are, to a first-order, independent of the interrogation waveform classification (i.e., pulsed or CW). The results from recent field measurements using a doublet-pulse and CW lidar are presented.

Form SF298 Citation Data

Report Date ("DD MON YYYY") 00042001	Report Type N/A	Dates Covered (from... to) ("DD MON YYYY")

Title and Subtitle Noise Mechanisms Impacting Micro-Doppler Lidar Signals: Theory and Experiment	Contract or Grant Number
	Program Element Number

Authors Gatt, Philip; Henderson, Sammy W.; Thomson, J. Alex; and Hannon, Stephen M.	Project Number
	Task Number
	Work Unit Number

Performing Organization Name(s) and Address(es) Coherent Technologies, Inc. 655 Aspen Ridge Dr. Lafayette, Colorado	Performing Organization Number(s)

Sponsoring/Monitoring Agency Name(s) and Address(es)	Monitoring Agency Acronym
	Monitoring Agency Report Number(s)

Distribution/Availability Statement
Approved for public release, distribution unlimited

Supplementary Notes

Abstract

Subject Terms

Document Classification unclassified	Classification of SF298 unclassified
Classification of Abstract unclassified	Limitation of Abstract unlimited
Number of Pages 15	

1. INTRODUCTION

The capability of micro-Doppler sensors have been the subject of various studies in the recent past. High-performance micro-Doppler sensors are planned for a variety of military and commercial applications. The primary military applications include characterization and identification of ground and airborne targets and battle damage assessment.

CTI has been actively involved in the development of eye-safe, solid-state 2μm coherent micro-Doppler laser radar sensors to measure the vibration spectra of distant hard targets. The waveform of these sensors span a variety of formats, which include CW, doublet-pulse, and agile pulse waveforms. Multi-pixel coherent array micro-Doppler sensors are also being developed. CTI has recently demonstrated the first pulsed-laser vibration sensor for micro-Doppler applications. For these measurements a doublet-pulse waveform was chosen. CTI is currently pursuing the development of more complex pulsed formats (triplet, quadruplet, and agile-pulse waveforms).

The velocity measurement precision of these sensors is governed by a variety noise sources, which include shot-noise, local-oscillator frequency noise, speckle decorrelation noise and refractive turbulence piston noise. The shot-noise (i.e. photon noise) represents the theoretical lower bound on the velocity measurement precision. The other noise sources add to this lower bound. In Section 2, we present the basic theory, which describes these noise sources and their wavelength dependence. Data from simulations and real measurements are provided to substantiate the theory. In Section 3 we present results from a recent short and long range ground-based measurement campaign using both a doublet-pulse and CW micro-Doppler lidar sensor.

2. THEORY

2.1. Doublet-Pulse Waveform

The doublet-pulse or pulse-pair waveform is a limiting case of a general class of pulsed waveforms. It is routinely used in Doppler radar for both hard target and aerosol target applications. The pulse pair and poly-pulse-pair transmit formats have been applied to microwave radar for radial velocity and spectral width probing of weather echoes.[1] CTI has pioneered the development of the pulse-pair waveform for lasers using eyesafe, near-infrared optical wavelengths, and is in the process of developing agile versions (adaptive multiple pulse) of these transceivers for multi-function remote sensing applications.

The doublet-pulse provides coherent Doppler lidar systems a substantial time-bandwidth (TB) product of 10,000 or more enabling simultaneous high resolution range and precision velocity measurement capability, with a very modest processing, data throughput, and storage requirements. Figure 1 illustrates the doublet-pulse waveform format. The waveform comprises a pair of pulselets, each of duration τ, separated by T_s seconds. The range resolution of the lidar measurement is governed by the pulselet duration τ, while the velocity precision varies, to a first order, as the reciprocal of the pulselet separation, T_s. Ambiguities in the velocity measurement arise as a result of the periodic structure of the waveform. The velocity ambiguity interval is given by $V_a = \lambda/2T_s$, where λ is the operating wavelength. These ambiguities can be readily dealt with in software in many applications. Higher order variants of the general doublet-pulse (e.g., the triplet-pulse) would also help eliminate such ambiguities.

---

[1] Zrnic, D.S., "Estimation of spectral moments for weather echoes," *IEEE Trans. Geosci. Electron.* **GE-17**, 113 (1979).
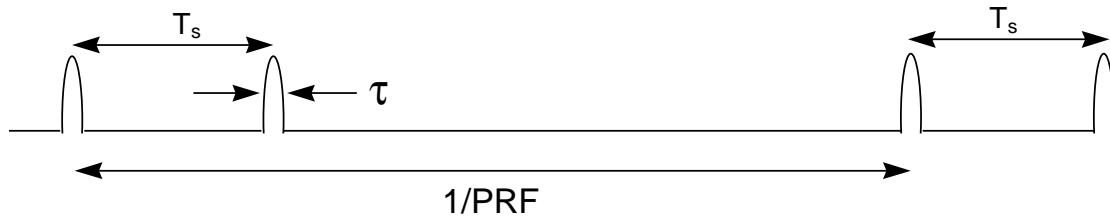
Figure 1: General doublet-pulse format

Unlike radar, the frequency and phase of the transmitted waveform are not constant from one laser pulselet to the next. Enhancements to the radar pulse-pair algorithm, developed at CTI, have solved this problem. The lidar doublet-pulse algorithm corrects for the random phase and frequency of the individual pulselets from measures of the transmitted pulselets called "monitor" samples. With these monitor samples the potential errors from arbitrary phase relationships (phase or frequency offset and chirp) between the pulselets are easily mitigated in the lidar algorithm.

The general doublet pulse coherent lidar concept provides a truly novel, robust sensor architecture that can be applied across a broad range of applications and operating wavelengths. It enables extremely efficient, low cost processing architectures for very high TB waveforms. Figure 2 provides a simplified illustration the doublet-pulse measurement process. The doublet-pulse waveform essentially measures the target velocity by measuring the phase change between the first and second pulselet caused as the range to target is increased or decreased by an amount $V \cdot T_s$, where V is the target velocity. In Figure 3 we provide sample doublet-pulse lidar signals from a pair of range-resolved targets (one stationary and one vibrating). This figure illustrates the doublet-pulse measurement process and its potential for combined high-resolution range and precision velocity measurements.
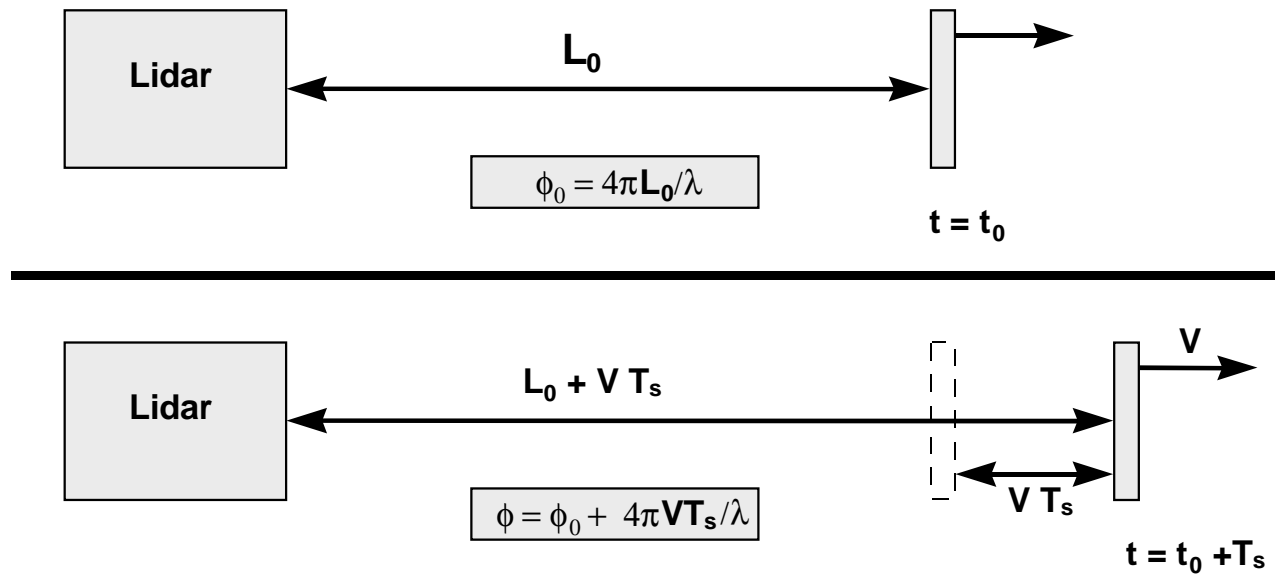

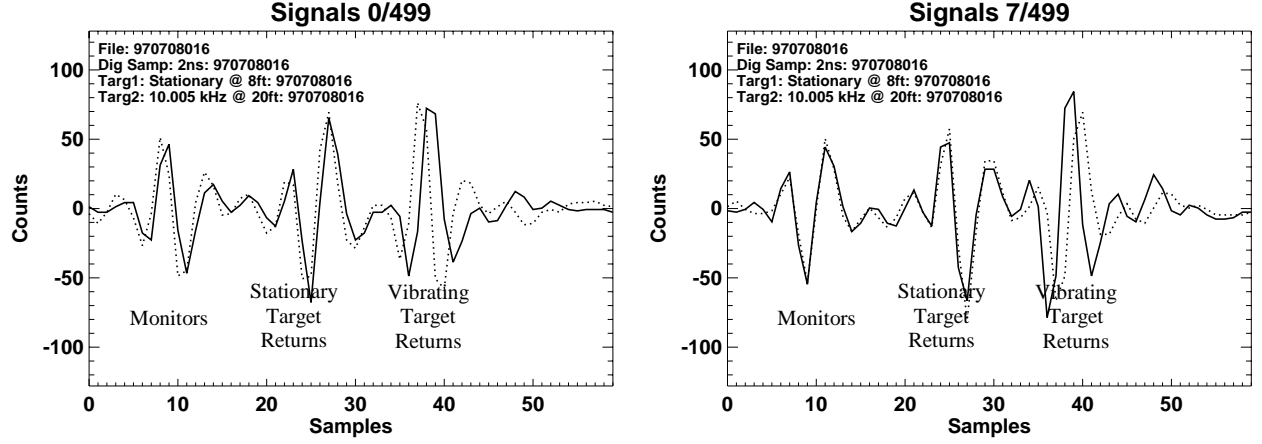**Figure 2: Principle of velocity measurement with the pulsed waveform**

Figure 3: Example dual target doublet-pulse RF signals
Selected doublet pulse monitor signals and returns from a pair of range-resolved targets: first pulselet (solid) and second pulselet shifted in time (dash). The selected samples were chosen such that the two monitor signals exhibit a near zero phase difference. The first target is stationary and its returns exhibit a net phase difference equal to the phase difference of the two monitor signals. The second target was vibrating at 10.005 kHz. The relative phase relationship of the second target returns are non-zero and are a function of the target velocity and pulselet separation time.

2.2. Composite Velocity Precision

There are a variety of sources that introduce noise into the velocity measurement process. These noise sources are present regardless of the waveform format (general-pulse, doublet-pulse, CW, etc.). Some of these noise sources include photon noise, signal coherence noise, local oscillator phase or frequency noise, and refractive turbulence induced piston noise. The composite effect these noise sources are modeled as the RMS sum of the noise from each source. That is

$$\sigma_V = \sqrt{\left(\sigma_{V_{sn}}^2 + \sigma_{V_{coh}}^2 + \sigma_{V_{LO}}^2 + \sigma_{V_{turb}}^2 + ...\right)\Big/N} \quad . \tag{1}$$

Where σ_V is the velocity measurement precision and N is the number of independent waveforms averaged. In the limit of large noise, the doublet-pulse velocity precision saturates to a level given by $\sigma_{Vsat} = V_a/\sqrt{12}$. Where $V_a = \lambda/2T_s$ is the velocity ambiguity interval. This result is a consequence of uniformly distributed velocity noise over the ambiguity interval. For a CW waveform the corresponding velocity interval is the velocity search bandwidth (typically half the data sample frequency). The effect of this precision saturation can be included in the velocity precision model, via

$$\sigma_{V_{w/sat}}^{-2} = \sigma_{V_{sat}}^{-2} + \sigma_V^{-2} \tag{2}$$

In the following subsections we provide theoretical descriptions of these noise terms and real or simulated data, which substantiates or validates the theory.

2.3.   Photon or Shot-Noise (CRLB)

For a coherent detection receiver, photon (shot) noise represents the fundamental lower bound on velocity estimation precision. This limit is called the Cramer-Rao lower bound (CRLB). Van Trees[2] provides a general formula for this lower bound for an arbitrary waveform. His expression can be written as

$$\sigma_{V\,sn} \geq \frac{\lambda}{4\pi\sqrt{2}\sigma_t} \frac{\sqrt{(1+\gamma)}}{\gamma} . \tag{3}$$

Where γ is the waveform's Carrier-to-Noise Ratio (CNR) and σ_t is the standard deviation of the intensity waveform or the waveform "effective duration."   For a high time-bandwidth product doublet pulse waveform, the effective duration can be shown to be ~ $T_s \sqrt{[A(1-A)]}$, where A is the ratio of the intensity of one of the pulselets to the total intensity.   The term $\sqrt{[A(1-A)]}$ is the geometric mean of the two fractional intensities. When $A = 1/2$ the effective duration is $T_s/2$. Using this result, the CRLB for the a high time-bandwidth product doublet-pulse waveform is given by

$$\sigma_{V_{sn}|\gamma} = \frac{\lambda}{4\pi\sqrt{2A(1-A)}T_s} \frac{\sqrt{(1+\gamma)}}{\gamma} = \frac{\lambda}{4\pi\sqrt{2}T_s} \frac{\sqrt{(1+\gamma)}}{\sqrt{\gamma_1\gamma_2}} . \tag{4}$$

Where, γ_1 and γ_2 are the CNR of the first and second pulselets. In the left panel of Figure 4 we present the results of a Monte Carlo simulation of the doublet pulse algorithm.   The simulation consisted of generating 10^4 pulse-pair waveforms each with a constant amplitude and random Gaussian shot-noise to affect a prescribed CNR. The circles in the plot represent Monte Carlo simulation results. The solid lines represent the CRLB modified to include the effect of saturation (i.e. Eq 2) for each of four levels of waveform averaging ($N = 1, 3, 10$ and 100). As can be seen in the data, the simulation results agree with the theory. Also shown on the plot are results from lidar measurements. This data is indicated by the plus (+) symbols. This data is in close agreement with the theory. Part of the bias is from an energy imbalance ($A = 2/3$) and other systematic errors. At high CNR the lidar data saturates due to a finite monitor CNR of ~ 30 dB.

In the right panel of Figure 4, we present results when the signal amplitudes were randomized according to a Rayliegh distribution, corresponding to an exponentially distributed signal intensity.   This distribution is typical for speckled lidar returns in the absence of refractive turbulence. The theoretical curves (solid lines) take into account the fluctuations of the CNR about the mean $<\gamma>$ for an exponentially distributed intensity. The theoretical model incorporates the effect of variable waveform intensity via conditional statistics. Accordingly, the standard deviation of the velocity estimates are given by

$$\sigma_{V_{sn}} = \sqrt{\int \sigma^2_{V_{sn}|\gamma}\, p_\gamma(\gamma)\,d\gamma} . \tag{5}$$

Where, $\sigma^2_{v|\gamma}$ is the conditional velocity measurement variance (i.e., the CRLB of Eq. 4 modified to include the effects of velocity noise saturation over the ambiguity interval via Eq. 2) and of $p_\gamma(\gamma)$ is the probability density function of the CNR. For variable degrees of averaging, N, the statistics of the averaged intensity are no longer exponentially distributed.   Instead the average intensity follows a Gamma distribution, which is given by

$$p_\gamma(\gamma) = (N/\langle\gamma\rangle)^N \gamma^{N-1} e^{-N\gamma/\langle\gamma\rangle} / \Gamma(N) . \tag{6}$$

---

[2] Van Trees, H. L., Eq. 10.95, Detection, Estimation, and Modulation Theory, Part III: Radar-Sonar Signal Processing and Gaussian Signals in Noise, John Wiley & Sons, New York, 1971.

Where $\Gamma(x)$ is the gamma function. Eq 5 was evaluated numerically to generate the theoretical curves shown in the right panel of Figure 4. As can be seen there is good agreement between the numerically evaluated theory and the Monte-Carlo simulations (circles on the curve). For moderate to large number of averages (N > 5) there is virtually no difference between the fading and non-fading velocity precision. For single waveform averaging, the velocity precision of the lidar returns from a diffuse-target (fading) is approximately 2.5 times larger than that from a specular target (non-fading), for a CNR in range of 20 to 40 dB.
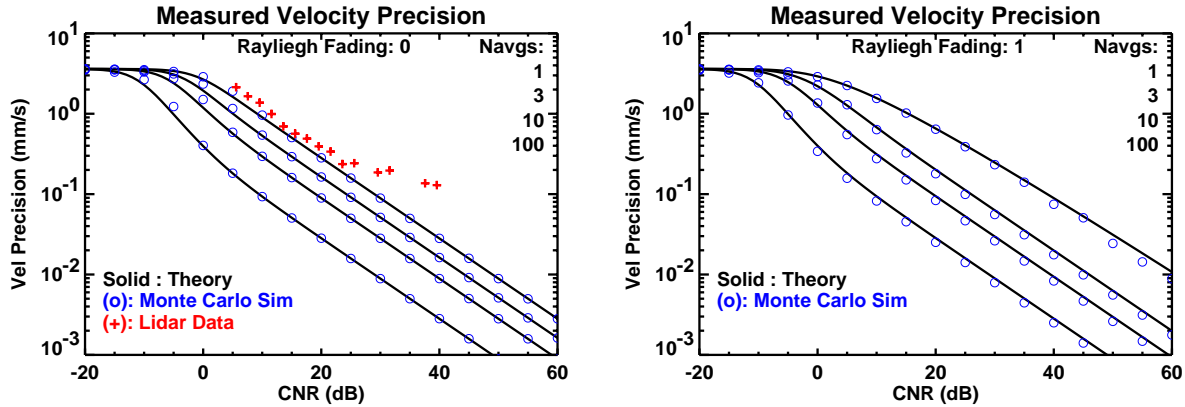
Figure 4: Doublet-pulse velocity precision for a glint and diffuse target.
Velocity precision as a function of the CNR and the degree of signal averaging, *N*, for a 2 μm doublet pulse transceiver with 80 μs pulselet separation: without (left) and with Rayleigh fading (right). Circles indicate results from Monte Carlo simulations, plus symbols are results from lidar measurement and solid lines are theory.

2.4. Target Decorrelation Noise

Target decorrelation or coherence noise can result from a variety of target mechanisms. For example target rotation or translation results in speckle translation and/or boiling. This decorrelation results in a broadening of the signal spectrum, which introduces noise in the velocity estimation process. Since finite signal coherence results in saturation of the velocity precision that can be obtained in a single signal coherence time, CNR in excess of about 10 dB does not provide significant. The design of a lidar aimed at the best velocity precision is one, which is able to adapt to achieve a CNR in the 10 dB range. If excess power is available, it is better to use this power to make more measurements (transmit more pulses) in order to benefit from increased averaging to improve the velocity measurement precision by √N. If a cw lidar has CNR in the 0-10 dB range then it will provide the best measurement precision since it can make the maximum number of coherent measurements in the measurement dwell time. An optimally designed pulsed system with one or more pulse pairs per signal coherence time will achieve a similar velocity measurement precision. In cases where the cw CNR is below 0-10 dB an agile pulsed lidar – one that can lower the PRF and increase the energy per pulse-- will allow the CNR to be increased to 0-10 dB allowing better precision.

For the pulse-pair waveform, the velocity precision as a function of CNR and signal coherence has been derived by Zrnic[3].

[3] R. J. Doviak and D. S. Zrnic 'Doppler Radar and Weather Observations', Academic Press 1984, Eq. 6.22b

$$\sigma_{V_{Zrnic}} = \frac{\lambda}{4\pi\sqrt{2}T_s\rho_V(T_s)}\sqrt{\left(\frac{\gamma/2+1}{\gamma/2}\right)^2 - \rho_V^2(T_s)} \tag{7}$$

Where, $\rho_v(\tau)$ is the velocity autocorrelation function given by

$$\rho_V(T_s) = \exp(-T_s^2/T_c^2) \tag{8}$$

and T_c is the signal coherence time. Zrnic's expression takes into account both signal decorrelation and photon-noise given by the CRLB. Using the formalism defined in Eq 1, we can rewrite Zrnic's expression as the RMS sum of the photon or shot-noise term and the coherence term. That is

$$\sigma_{V_{Zrnic}} = \sqrt{\sigma_{V_{sn}}^2 + \sigma_{V_{coh}}^2} \tag{9}$$

Solving for the coherence term yields

$$\sigma_{V_{coh}} = \frac{(1+2/\gamma)\lambda}{4\pi\sqrt{2}T_s}\frac{\sqrt{1-\rho_V^2(T_s)}}{\rho_V(T_s)} \tag{10}$$

Which has a weak dependence on the CNR. This dependence is thought to be an artifact of approximations imposed in Zrnic's formula. For small T_s/T_c and CNR $>> 1$, the pulse-pair velocity precision is well approximated by

$$\sigma_{V_{coh}} \approx \frac{\lambda}{4\pi T_c} \tag{11}$$

In Figure 5 we plot Zrnic's formula for the pulse-pair mean velocity estimation precision normalized by the true velocity standard deviation vs the ratio of the pulselet separation time to the signal coherence time T_c. There is an optimum pair spacing or sampling interval that yields minimum error. The diamonds in the figure indicates this optimal spacing. For the pulse-pair waveform, the increase of error at large pair spacing is due to loss of coherence between the two samples. On the other hand, at too small a spacing the precision of the estimate is dominated by the CRLB. Minimum error is achieved by spacing the pairs to be about 65% of the coherence time near a CNR of 10 dB and at a smaller fraction at high CNR.

Equation 7 (Figure 5 right panel) shows that in order to obtain performance within a factor of two of the velocity saturation value , $\sigma_{Vcoh} = \lambda/4\pi T_c$, due to the finite signal coherence, then the CNR should be greater than ~6 dB and the pulse spacing optimized. For operationally relevant CNRs in the 0-10 dB range, the pulse spacing, T_s, should be nominally within the range of $0.2T_c - 1.2\ T_c$ in order to achieve performance that is within a factor of two of the performance achieved at the optimal spacing. For CNRs greater than 10 dB the requirement on the lower limit of the pulse spacing is further relaxed (e.g., at 40 dB, near optimal performance is obtained with pulse separations over the two orders of magnitude between ~ $0.01\ T_c - T_c$ range).
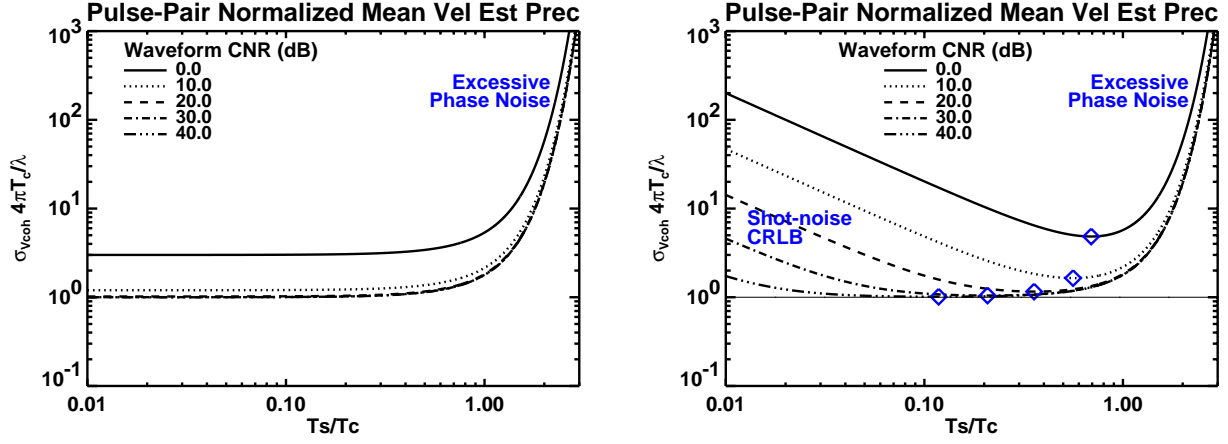
Figure 5: Velocity estimate precision for the doublet-pulse waveform
Pulse-pair velocity estimate precision normalized by ($\lambda/4\pi T_c$) vs. the ratio of the pulselet separation time to the coherence time. Precision due to signal decorrelation alone (left) and combined with CRLB (right). The diamonds indicate optimal values of the ratio of the separation time to the coherence time.

The inverse linear dependence on of the velocity precision on the coherence time has been verified with CW lidar measurements of a resolved rotating target. For a Gaussian beam illumination the velocity distribution has a Gaussian shape given by

$$f_V(V) = k \exp(-2(V/\Omega\omega_b)^2) = \left(2\pi\sigma_{V_{coh}}^2\right)^{-1/2} \exp(-V^2/2\sigma_{V_{coh}}^2). \qquad (12)$$

Where, k is a constant of proportionality. Therefore the velocity standard deviation is given by

$$\sigma_{V_{coh}} = \Omega\omega_b/2 \approx \Omega\lambda R/2\pi\omega_o. \text{ For a well resolved rotating target} \qquad (13)$$

Where ω_o is the transmit beam radius. The coherence time is therefore given by

$$T_c = \lambda/2\pi\Omega\omega_b = \omega_o/2\Omega R. \text{ For a well resolved rotating target} \qquad (14)$$

Equation 13 is plotted in Figure 6 along with CW lidar velocity precision estimates. The data fits extremely well to the model. For a highly unresolved rotating target ($D_t << \omega_b$), the velocity distribution is governed by the target diameter D_t rather than the beam diameter. Consequently, the velocity precision becomes both wavelength and range independent. An approximate formula for this condition is given by

$$\sigma_{V_{coh}} = \Omega D_t/2. \text{ For a highly unresolved rotating target.} \qquad (15)$$

In the transition between resolved and highly unresolved there is a smooth transition from equation 13 to equation 15.
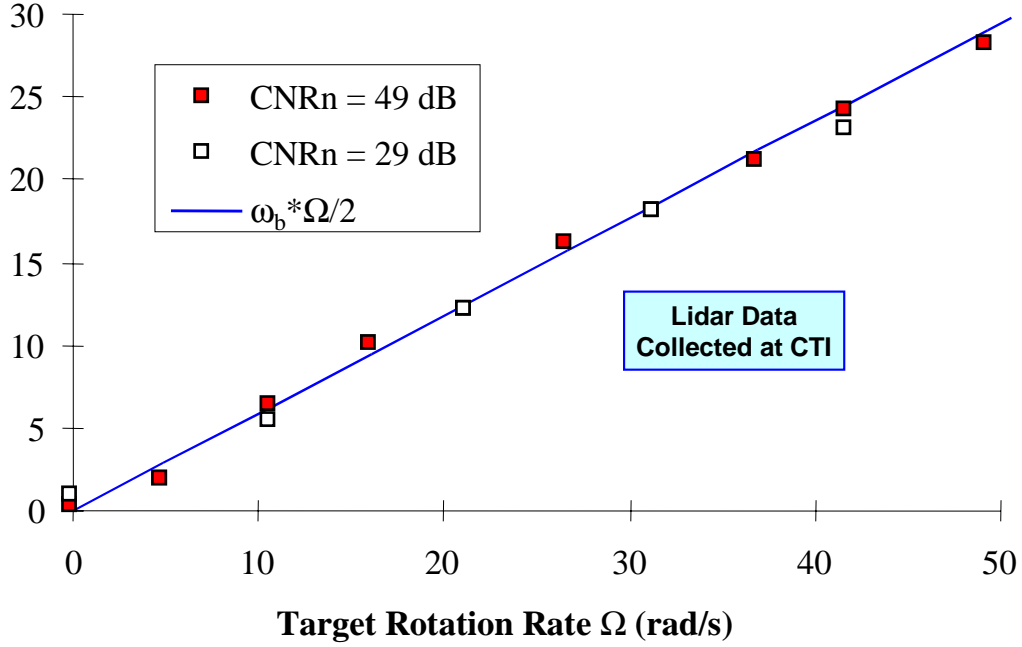
Figure 6: CW lidar velocity measurement precision of a resolved diffuse target rotation
Velocity measurement precision from CW lidar for a resolved diffuse target under relatively high CNR conditions, when the processing dwell time was fixed to a time less than the signal coherence time; ω_b is the $1/e^2$ beam radius on the resolved target and Ω is the target rotation rate, which is proportional to the inverse of the coherence time.

2.5. Local Oscillator Laser Frequency Noise

Local oscillator frequency noise is another source, which can degrade the velocity precision of a coherent lidar. The relevant parameter is the change in frequency as a function of target round-trip time. One measure of this frequency noise is the root of the frequency deviation structure function $D_{\delta f}(\tau)$. The structure function provides information about the frequency deviation as a function of delay time. It is defined as the expected value of the square difference of the frequency-deviation δf from itself delayed in time.

$$D_{\delta f}(\tau) = \left\langle [\delta f(t) - \delta f(t-\tau)]^2 \right\rangle. \tag{16}$$

$$D_{\delta f}(\tau) = 2\sigma_{\delta f}^2 - 2R_{\delta f}(\tau). \tag{17}$$

Where $R_{\delta f}(\tau)$ is the autocorrelation function of δf. Therefore, the structure function is directly related to the Fourier Transform of the Power Spectrum. From Eq 17 we see that at long delays the structure function saturates at twice variance of the frequency deviation. It therefore makes sense to define the square root of the structure function divided by two as the delay-dependent standard deviation of the frequency deviation. That is

$$\sigma_{\delta f}(\tau) = \sqrt{D_{\delta f}(\tau)/2}. \tag{18}$$

When the signal to be analyzed is the result of the beating of two CW lasers (each assumed to have identical frequency statistics), one can expect that the delay-dependent frequency standard deviation of

one of the lasers is that of Eq 17 divided root(2). Therefore we estimate the delay dependent velocity precision contribution from the local oscillator as

$$\sigma_{V_{LO}}(\tau) = \sigma_{\delta f}(\tau)\,\lambda / 2\sqrt{2}\,. \tag{19}$$

In Figure 7 we present the frequency deviation vs. time of the beat signal between two different local oscillators (left panel) and the corresponding velocity estimate precision (right panel). This data suggests that the long-term rms frequency noise is ~ 20 kHz and at a delay of 10 μs it is ~ 1.8 mm/s. The frequency measurement noise for this data set is estimated to be ~ 90 Hz.
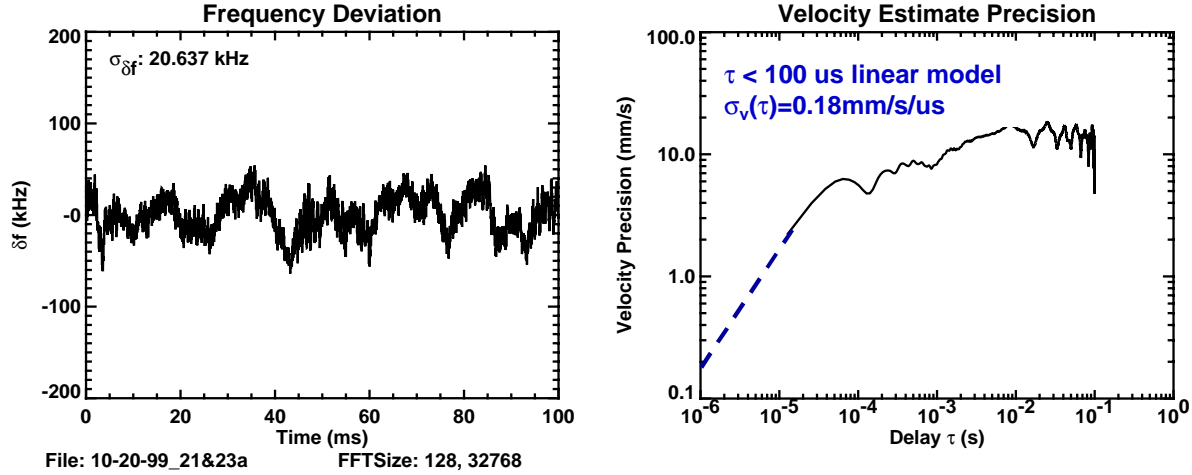
Figure 7: Measurements of the frequency deviation of the beat frequency between two diode-pumped CW 2μm local oscillators.
Frequency deviation vs. time (left panel) and the root velocity structure function divided by four (right panel). The signal CNR was ~ 36 dB. The data was processed with a processing dwell time of 12.8 μs corresponding to a estimated measurement precision of 90 Hz.

The data presented in the figures above corresponded to the beating of two CW local oscillator lasers. From this data, it is impossible to determine the relative contribution of each laser to the composite noise spectrum. One technique to measure of the frequency noise of a single source is the so called "Delayed Self Offset Homodyne" technique. However, for this technique to be viable, a relatively long ~ 10 μs noiseless delay line is required. For a 1.5 μm laser, a 1 km fiber delay line can be utilized for this measurement. However at 2μm, the fiber extinction loss in glass fiber is large for lengths on the order of 1 km.

Another method to measure the effect of local oscillator noise of a single source is to use an atmospheric delay line, presuming refractive turbulence and photon noise are significantly lower than the local oscillator noise. The data in Figure 8 is an example of two velocity measurements of a stationary target at 7.5 km (50 μs delay). This data suggests that the local oscillator noise is the dominant noise source in the measurement, because it was reduced by a factor of two by employing a quieter laser controller. The level of frequency noise in this data is ~ 2 kHz (left panel) and 0.9 kHz (right panel). In the next section we show that refractive turbulence piston noise was negligible compared to the measured velocity noise.

The structure function suggests the velocity precision is linearly related to the delay time for small delays. The data from the quieter controller suggests a constant of proportionality of 19τ m/s^2.

$$\sigma_{V_{LO}}(\tau) = 19\tau\,(m/s^2) \ \ (\text{for } \tau \ll 100\ \mu s) \tag{20}$$
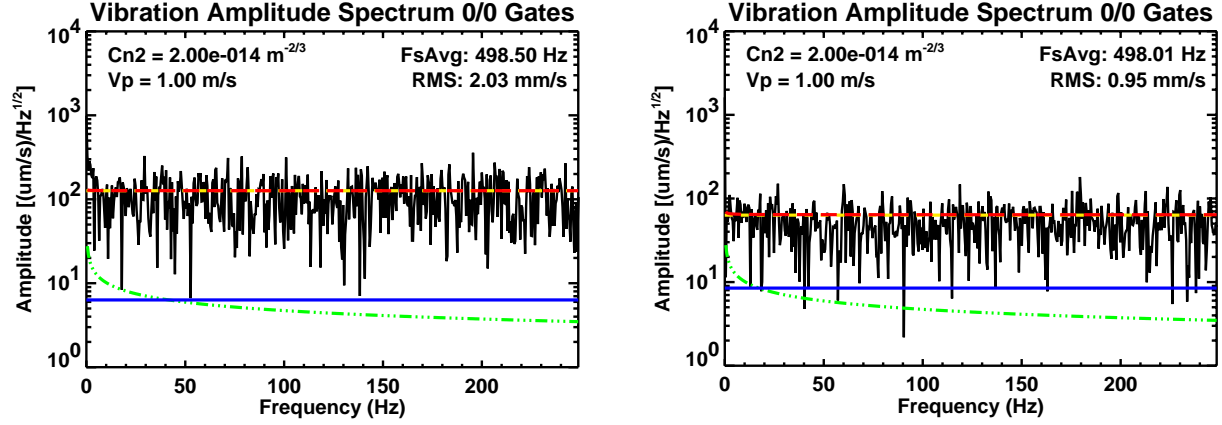
Figure 8: Long-range doublet-pulse velocity measurements of a stationary target
Doublet-pulse velocity measurements of a stationary target at 7.5 km (50 μs delay) using two different local-oscillator controllers with a single local oscillator. CTI controller number 23 demonstrating ~ 2 mm/s rms velocity noise (left panel) and controller number 21 demonstrating ~ 0.95 m/s rms velocity noise (right panel). Estimated LO frequency noise (short-dash), refractive turbulence piston noise (dot-dot-dot-dash), photon noise (solid) and cumulative noise (long-dash). The mean CNR in this data set was approximately 40 dB and the pulselet separation time was ~ 40μs. This data suggests that the velocity noise at 7.5 km is dominated by local oscillator noise. The refractive turbulence piston velocity noise level is estimated to be approximately an order of magnitude less.
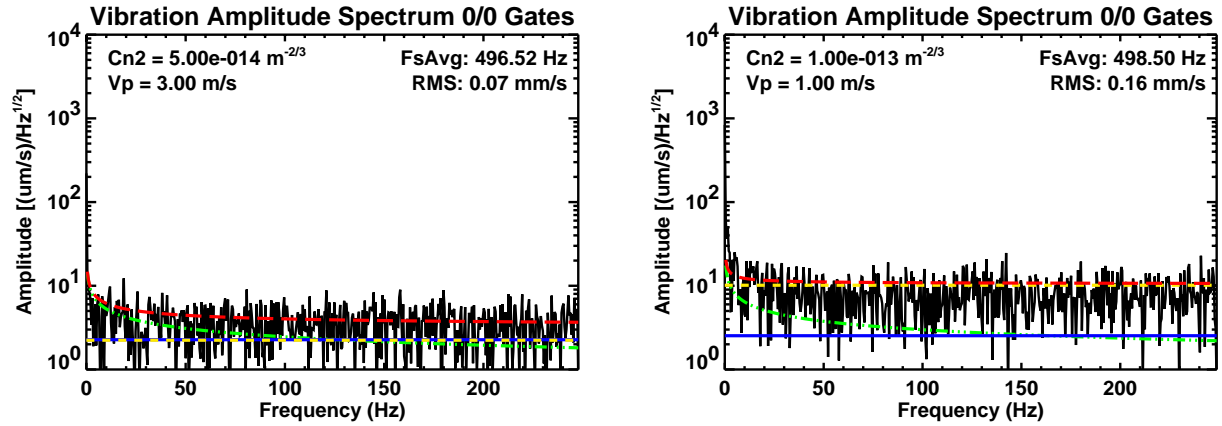

Figure 9: Short-range Doublet-pulse velocity measurements of a stationary target
Doublet-pulse velocity measurements of a short range stationary target (100 m left and 600 m right) using controller number 23. Estimated LO frequency noise (short-dash), refractive turbulence piston noise (dot-dot-dot-dash), photon noise (solid) and cumulative noise (long-dash). The mean CNR in this data set was approximately 40 dB and the pulselet separation time was ~ 85μs. This data suggests that at short range (130 m) all three noise sources contribute equally, while at 600 m the LO frequency noise dominates and that the linear model of Eq. 20 is reasonably valid.

2.6.   Refractive Turbulence Piston Noise

Advection of patterns of spatial fluctuations of temperature or humidity across the lidar beam can result in a time varying optical path length between the lidar and the target under observation. The rate of change

of these variations appears in the Doppler signal as an apparent motion of the target in the lidar direction. Ishimaru[4] has carried out an analysis of these effects on the phase of a coherent laser signal assuming that a Kolmogorov turbulence field of refractive index variations is being advected across the beam by the local wind or by the beam motion itself. His results can be expressed in terms of the power spectrum of apparent target velocity fluctuations ($\Phi(\omega)$ in m^2/s^2/Hz) according to

$$\Phi(\omega) = \frac{10.9}{\omega^{2/3}} \int_{r_1}^{r_2} V_p(r)^{5/3} C_n(r)^2 dr .$$

(21)

Where $V_p(r)$ and $C_n^2(r)$ are the transverse component of the wind and the refractive index structure constant respectively at the distance r along the line of sight and ω is the (radian) frequency. For constant C_n^2 and V_p the integral can be solved analytically in terms of the path length, L.

$$\Phi(\omega) = \frac{10.9 V_p^{5/3} C_n^2 L}{\omega^{2/3}} \quad \text{and} \quad \sigma_{V_{turb}} = \sqrt{\int \Phi(f) df} \quad \text{with } f = 2\pi\omega.$$

(22)

In Figure 10, we present the vibration amplitude spectra form doublet-pulse measurements taken on two consecutive days of a target at ~ 250m and overlay the above model for the velocity noise due to refractive turbulence piston effects. In the left panel the wind conditions were calm and the noise is seen to exceed the turbulence model across the entire frequency band. The right panel corresponds to data taken under windy conditions (V_p ~ 10 m/s). At frequencies below 10 Hz, the turbulence model fits well to the elevated noise floor seen in the vibration spectra. Above 10 Hz the noise is dominated by local oscillator noise.
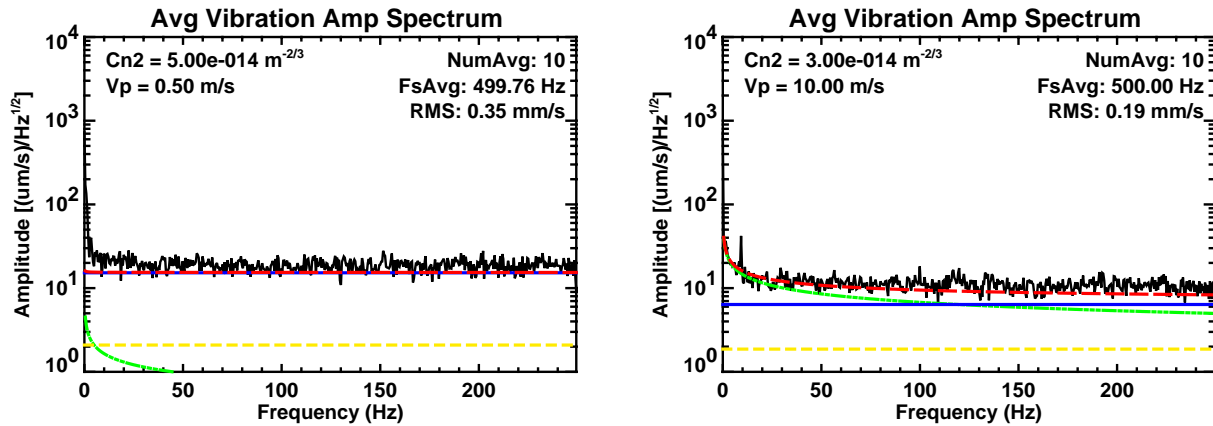

Figure 10: Doublet-pulse vibration spectra of a stationary target at ~ 250 m.
Doublet-pulse velocity amplitude spectra for a stationary target at ~ 250 m under calm conditions (C_n^2 ~ 5x10^{-14} m$^{2/3}$ and V ~ 0.5 m/s (left panel)) and windy conditions (C_n^2 ~ 3x10^{-14} m$^{2/3}$ and V ~ 10 m/s (right panel)) and an overlay of the expected LO frequency noise (short-dash), refractive turbulence piston noise (dot-dot-dot-dash), photon noise (solid) and cumulative noise (long-dash). At frequencies below 10 Hz, the turbulence model fits well to the elevated noise floor seen in the windy data (right panel). The frequency resonance at ~ 10 Hz is due to a vibration frequency of the target structure which was being driven by wind gusts.

[4] A. Ishimaru in Laser Beam Propagation in the Atmosphere, J. W. Strohbehn, ed.

3. EXPERIMENTS

The doublet-pulse transceiver was employed in an Air Force micro-Doppler measurement program. This program demonstrated the ability of the doublet-pulse concept to measure precision micro-Doppler vibration spectra. CTI measured the vibration spectra of an array of targets at both short and long range. For many of the short-range measurements a co-located CW vibrometer collected simultaneous vibration spectra. In the following sections we describe some of the results from these measurements.

3.1.   Short Range Micro-Doppler Measurements

The first set of measurements focused on short-range "proof of concept" measurements.   In this measurement campaign the vibration spectra from the doublet-pulse transceiver was compared to that collected using a CW vibrometer. Sample results are provided Figure 11 for a vibrating speaker and Figure 12 for the spectra of the door panel of a Toyota Celica at 2000 RPM is shown. Excellent agreement between the two sensors was obtained. The energy of the double-pulse transceiver was heavily attenuated to prevent receiver saturation. The data in the left panel of Figure 12 indicates a spectral noise floor on the order of 20 μm/s/root(Hz). This corresponds to a velocity precision of 316 μm/s, for the 250 Hz Nyquist bandwidth. The expected photon limited value assuming the measurement parameters (CNR_1 = 31.2 dB, CNR_2 = 29.9 dB, T_s = 40 μs, λ = 2 μm and Rayleigh fading) is 296 μm/s. The expected noise floor for the data in Figure 11 is about a factor of 2 less than the measured value. The difference is unexplained.
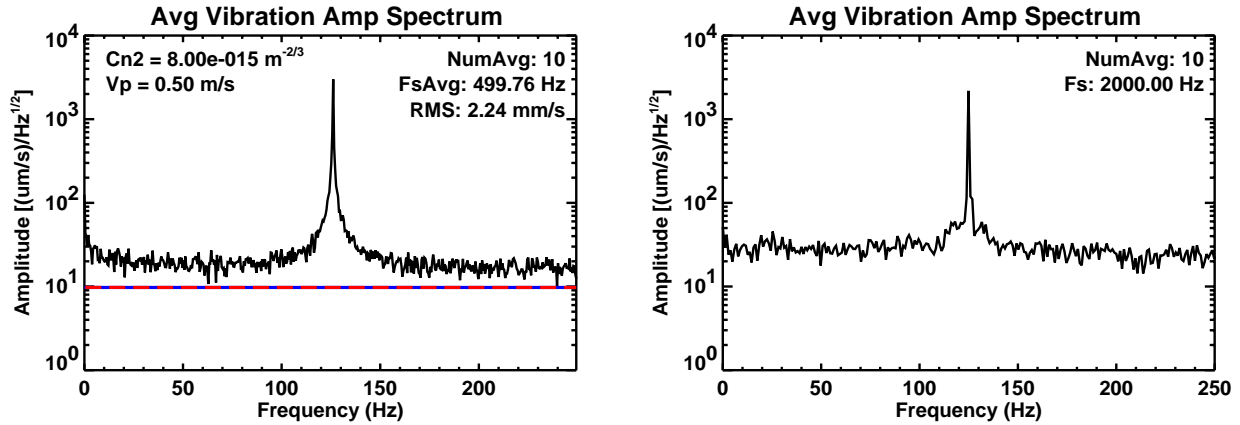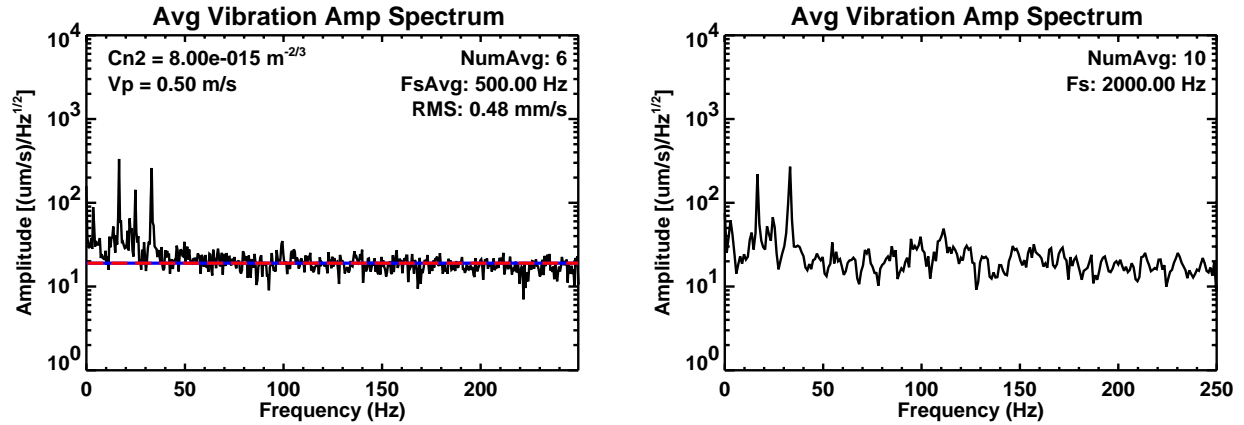

Figure 11: CW and doublet-pulse vibration spectra of a Toyota Celica at idle.
Doublet-pulse (left) and CW vibrometer (right) vibration spectra of an speaker vibrating at 4125 Hz. The doublet-pulse waveform PRF was 500 Hz and the CW lidar produced velocity estimates at 2 kHz. The expected value of the photon-shot noise is indicated by the straight line at ~ 10 μm/s/Hz1/2.

Figure 12: CW and doublet-pulse vibration spectra of a Toyota Celica at idle.
Doublet-pulse (left) and CW vibrometer (right) vibration spectra of an idling Toyota Celica at 43 m. The doublet-pulse waveform PRF was 500 Hz and the CW lidar produced velocity estimates at 2 kHz. The expected value of the photon-shot noise is indicated by the straight line at ~ 20 $\mu m/s/Hz^{1/2}$.

3.2. Long Range Micro-Doppler Measurements

The second set of measurements focused on long-range (~ 7.5 km) measurements. In this measurement campaign the vibration spectra of the engine of a Toyota Celica were obtained. Sample results are provided in Figure 13. The noise floor of ~ 100 $\mu m/s/root(Hz)$ is thought to be dominated by local-oscillator frequency noise, which is also the source of the 60, 120 and 180 Hz spectral peaks observed in the engine-off data (right panel of the figure).
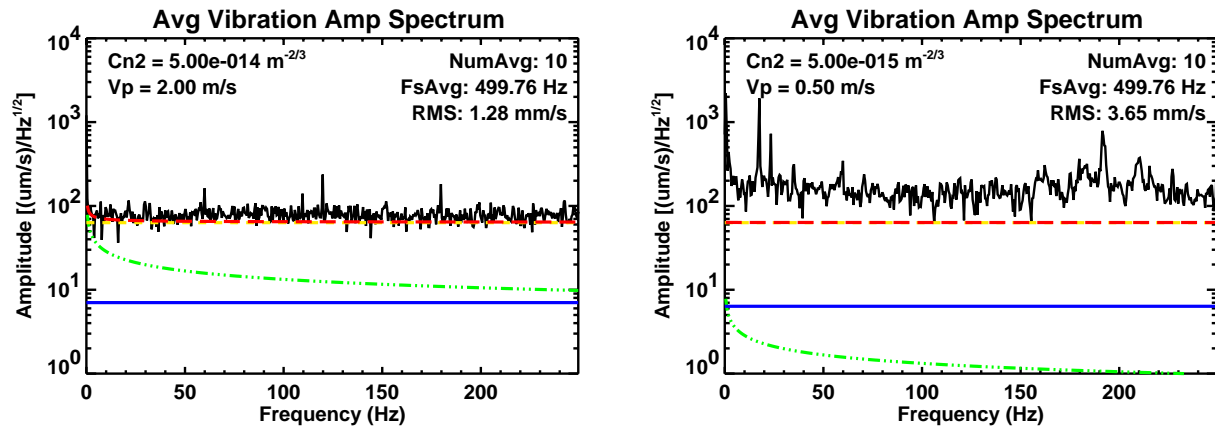

Figure 13: Doublet-pulse vibration spectra of the engine of a Toyota Celica at 7.5 km.
Spectrum of the engine off (left) and idling (right) with an overlay of the expected LO frequency noise (short-dash), refractive turbulence piston noise (dot-dot-dot-dash), photon noise (solid) and cumulative noise (long-dash). The noise floor is dominated by local-oscillator noise. The noise spikes at 60, 120 and 180 Hz are also from the local oscillator. The CNR was ~ 40 dB for both data sets.

4. SUMMARY AND CONCLUSIONS

Velocity precision models for micro-Doppler coherent laser radar sensors have been developed and verified with experimental and simulated data. The photon or shot-noise limited velocity precision was shown to be proportional to the illumination wavelength. A modified CRLB theoretical model was developed for the doublet-pulse waveform. This model was shown to agree with simulations for both constant and speckle fading signals. Speckle decorrelation models were shown to be proportional to the illumination wavelength, provided the target was well resoled. For an unresolved target the velocity noise depends upon the total spread of target velocities and is therefore both range and wavelength independent. An important parameter impacting the performance of the doublet-pulse waveform is the ratio of the pulselet separation time to the coherence time of the return signal. The optimum separation time was shown to be ~ 65 % of the correlation time, for weak 10 dB CNR conditions. A model for the impact of refractive turbulence noise was also developed. This wavelength independent model was shown to agree with experimental data.

Results from a recent, highly successful, micro-Doppler measurement campaign utilizing both a doublet-pulse and a CW transceiver were also presented. The CW and doublet-pulse micro-Doppler data were shown to be comparable. Doublet-pulse velocity precision estimates at short ranges agree well with photon limited noise estimates. At the present time the CW SNR is unavailable therefore nothing can be said about its velocity precision performance. Long range (~ 7.5 km) vibration spectra were also collected and agreed well with expectations. The velocity precision of the long-range measurements was shown to be dominated by local-oscillator frequency noise. CTI plans to develop active stabilization hardware to significantly reduce the level of local oscillator induced velocity noise.

5. Acknowledgements